

The Multivariate Extension of the Lomb-Scargle Method with its technical and astrophysical application

Martin Seilmayer

Ferran Garcia Gonzalez

Thomas Wondrak

October 26, 2022

Helmholtz-Zentrum Dresden - Rossendorf e.V., Institut für Fluidodynamik, Bautzner Landstraße 400, 01328 Dresden
m.seilmayer@hzdr.de

Abstract

The common methods of spectral analysis for multivariate (n -dimensional) time series, like discrete Fourier transform (FT) or Wavelet transform, are based on Fourier series to decompose discrete data into a set of trigonometric model components. The finite range of discrete data causes several limitations that originate from the orthogonality mismatch of the trigonometric basis functions on a finite interval. In the general situation of non-equidistant or fragmented sampling, FT based methods will cause significant errors in the parameter estimation. Therefore, the classical Lomb–Scargle method (LSM), which is not based on Fourier series decomposition, was developed as a statistical tool for one dimensional data. The present work generalizes LSM for n -dimensional data sets by a redefinition of the shifting parameter τ , to maintain orthogonality of the trigonometric basis. An analytical derivation shows that n -dimensional LSM extends the traditional 1D case preserving all the statistical benefits, such as consistency or the improved noise reduction. Here, we derive the parameter confidence intervals for LSM and compare it with FT. Astrophysical and experimental applications as well as ideal test data will illustrate and support the proposed method. Methods: data analysis, Techniques: spectroscopic, Sun: sunspots

1 Introduction

In many signal processing applications the power spectrum, or the amplitude and phase spectrum, of a physical process is of interest. Usually, the recorded signal is sampled in a finite equidistant time interval and stored as discrete data values. Typical applications of spectral analysis are the determination of characteristic frequencies, the appropriate choice of features in terms of frequency selection or suppression, as well as the precise measurement of amplitude and phase of a specific frequency. In most cases, such techniques rely on the discrete Fourier transform (DFT) or its fast version, the fast Fourier transformation (FFT). Both utilize the Fourier series to decompose the data into a set of coefficients from which the power spectrum can be deduced (Cohen 1995; Oppenheim 1999). These transformations are invertible, fast and easy to implement, but require equidistant sampling of the signal which is a hard restriction for scientific data, e. g. in astrophysics. From the well known one-dimensional case, DFT can be easily extended to higher dimensions. Here the image reconstruction for magneto-resonance tomography (Haacke 1999), image filtering (Gonzalez & Woods 2008) or higher order spectral filters in space and time (James 2011) represent just a few examples. Non-uniform sampling is utilized in the ultra fast nuclear magnetic resonance spectroscopy to gain a significant speed up for chemical analysis, see Frydman et al. (2003); Giraudeau & Frydman (2014). The cost of introducing a significant amount of missing values to a DFT procedure is a reduced sensitivity and loss of signal amplitude. The latter is a natural phenomenon of DFT or related procedures which deal with incomplete data sets and gaps, see Munteanu et al. (2016). However, the established meth-

ods for general sampling schemes like the “non-uniform Fourier transform”, e. g. Fessler (2002); Fessler & Sutton (2003); Liu & Nguyen (1998), still rely on classical orthogonal mode decomposition (application of FFT, DFT, Wavelet transform, etc.) with its systematical errors, as will be shown in Section 2.2.

The application of techniques based on Fourier series to signals with non-equidistant sampling is difficult, since it usually requires zero padding (replacing missing values by zeros) on a grid and in the general case resampling or interpolation of the data to a regular grid (Press & Rybicki 1989; Greengard & Lee 2004). The effect of a gap filling method is investigated extensively by Munteanu et al. (2016). Here, the conclusion is that without a corrective measure, errors such as amplitude minimization, which depends on the total gap density, cannot be avoided when FFT or DFT is applied. On the other hand, interpolation could be utilized to shift non-uniformly sampled data to a regular grid, so that the new interpolated data points are composed of the signal information and a projection of the accompanying noise. In the general case such distortions or noise are not band limited leading to biased estimates which consist of the local and aliased errors (noise, outliers, missing values, etc.) of the surrounding data.

Astrophysical data is often affected by gaps, missing values and unevenly sampling. For example, when ground based radio telescopes are exploring areas in space there might exist time intervals in which the antenna is not pointing towards the object of interest due to the rotation of the Earth. The result is an incomplete data set. Non-uniform (random) sampling emerges for example if the irregular appearance of objects like sunspots is measured as a binary quality depending on time and location. Section 4.3 provides a working example which analyzes frequencies and periods in latitude and time from the two dimensional data set of sunspot observations. An other technical example for random sampling (with highly variable sampling frequency) is asynchronous data acquisition in large sensor networks, which are used in Smart Home, Industry 4.0 and automated driving, see Geneva et al. (2018); Cadena et al. (2016); Sudars (2010). Here the time series provide missing values and data gaps originating from time periods, in which strong noise prevents the measurement or simply the source of the signal to be measured is not in the range of the sensor.

The Lomb-Scargle method (LSM) was developed especially for ground based non-uniformly sampled one dimensional data, from which the amplitude spectrum is calculated (Lomb 1976; Scargle 1982). The main advantage of this method is to directly estimate the spectrum without iterative optimization of trigonometric models as discussed in Section 2.1. A fast version for one dimensional signals is presented by Townsend (2010) and Leroy (2012).

An extension of LSM to two- or three-dimensional time series have not been presented yet. Especially for large multivariate data sets such a direct approach would be comparably faster than present iterative procedures as proposed in Babu & Stoica (2010, Chap. 9). The advantages of multivariate LSM will be demonstrated in Section 4 by means of a 3D Ultrasound flow profile measurement and the 2D analysis of sunspot time series data.

In case of the analysis of flow profile measurements which are obtained in an experiment investigating the magnetorotational instability in liquid metals (Seilmayer et al. 2014), such method would be highly desirable. Due to the complex experimental setup and the weak signal to noise ratio, the flow profile measurements contain several time intervals, in which distortions are dominant, see Seilmayer et al. (2016). These time intervals had to be rejected leading to a time series with invalid (missing) data points, from which the multivariate version of LSM is able to determine the parameters of the characteristic traveling wave.

In order to demonstrate the method and to motivate the basic idea of the multivariate version of LSM it is compared with the traditional orthogonal mode decomposition (OMD) with trigonometric basis functions, which is the essence of the classical Fourier transform, in terms of necessary conditions and error (noise) behavior. It will be shown that LSM fits better to the conditions of an arbitrary finite length of the sampling series in comparison to DFT, because LSM reduces the error in model parameter estimation. In contrast to the traditional approach, which was derived from a statistical point of view (see the appendix in J.D. Scargle Scargle (1982)), the presented method is deduced from a technical point of view and focuses on its application. This leads to a slight change in the scaling of model parameters, which will be discussed in Section 3.2. However, the introduced

procedure includes all benefits, like arbitrary sampling, fragmented data and a good noise rejection.

The starting point of this paper is the analysis of a continuous 1D signal $s : \mathbb{R} \rightarrow \mathbb{R}$ which is composed of an arbitrary and finite set of individual frequency components $\omega_i, 0 \leq i \leq M$. Without loss of generality, band limitation is assumed stating that there exists an upper maximum frequency ω_{\max} with $\omega_i < \omega_{\max}, 0 \leq i \leq M$, which mimics an intrinsic low pass filter characteristic of the measurement device. Since the measurement time is finite, the value of s is only known in the time interval $[0, T]$ with $T \in \mathbb{R}$ and $T > 0$. The m -dimensional extension of this signal is $S : \mathbb{R}^m \rightarrow \mathbb{R}$. If such a continuous signal is sampled, the pair $(\hat{s}_i, t_i) \in \mathbb{R}^2, 0 \leq i \leq N - 1$, represents the measured 1D value and the corresponding instant in time whereas the pair $(\hat{S}_i, \vec{t}_i) \in \mathbb{R}^{m+1}, 0 \leq i \leq N - 1$, represents a measured value and the m -dimensional location (space/time) for the i -th sample (N is the number of samples). All the methods presented in this paper are implemented in a package written in R and published on CRAN (Seilmayer 2019).

2 Mathematical model and comparison of OMD and LSM

In order to delineate the differences between trigonometric OMD and LSM, we start with the basic model of a periodic signal as a sum of signals of different frequencies $\omega_k, 0 \leq k \leq M$, with the corresponding amplitude $A_k \in \mathbb{R}$ and phase shift $\varphi_k \in \mathbb{R}$. The corresponding trigonometric model function

$$y(t) = \sum_{k=0}^M A_k \cos(\omega_k t + \varphi_k) \quad (1)$$

$$= \sum_{k=0}^M (a_k \cos(\omega_k t) + b_k \sin(\omega_k t)) \quad (2)$$

describes an infinite, stationary and steady process $y : \mathbb{R} \rightarrow \mathbb{R}$ with the coefficients $a_k, b_k \in \mathbb{R}$ for the defined frequency ω_k and the identities $A_k = \sqrt{a_k^2 + b_k^2}$ as well as $\varphi_k = \tan^{-1}(b_k/a_k)$. Furthermore, the trigonometric model above consists of an arbitrary number $M \in \mathbb{N}_0$ of frequency components. If the given signal $s(t)$ is described by the defined model from Eq. (2) the model

misfit ϵ is given by

$$\epsilon(t) = s(t) - y(t). \quad (3)$$

Thus, the signal can now be described by inserting Eq. (2) into Eq. (3) and defining the misfit ϵ_k for each discrete frequency k with $\epsilon(t) = \sum_k \epsilon_k(t)$ as follows:

$$s(t) = \sum_{k=0}^M (a_k \cos(\omega_k t) + b_k \sin(\omega_k t) + \epsilon_k(t)). \quad (4)$$

The defined misfit originates from measurement uncertainties or parametric errors from a_k, b_k . In the general case $\epsilon(t)$ can be any function or distribution. The challenge is to precisely determine the model parameters a_k and b_k for a given signal $s(t)$ achieving minimal $\epsilon(t)$. This can be accomplished by one of the following three methods: (i) Least-Square fit; (ii) orthogonal mode decomposition; (iii) Lomb-Scargle method (LSM).

2.1 Approach i – Least square fit

The optimal fit is reached by least square fitting, resulting in a minimum ϵ , which was shown by Barning (1963); Mathias et al. (2004). Since such procedures are iterative, the convergence of the algorithm might need a large number of function evaluations of Eq. (4). Therefore, a direct version like LSM is preferable. It can be shown that LSM becomes equivalent to a least square fit of a sinusoidal model (Lomb 1976; Barning 1963).

2.2 Approach ii – Trigonometric OMD

Generally, two functions $f, g : \mathbb{R} \rightarrow \mathbb{R}$ are said to be orthogonal on the interval $[a, b] \subset \mathbb{R}$, if the following condition holds, refer to Weisstein (2019):

$$\int_a^b f(x)g(x) dx = 0. \quad (5)$$

By selecting $f(x) = \sin(x)$ and $g(x) = \cos(x)$, the integration leads, by exploiting the identity $\cos(x) \sin(x) = \frac{1}{2} \sin(2x)$, to

$$\frac{1}{4} (\cos(2a) - \cos(2b)) = 0, \quad (6)$$

which is only zero, if $\cos(2a) = \cos(2b)$. This is true for any $a \in \mathbb{R}$, if the length of the interval $[a, b]$ is a multiple

of the period 2π so that $2b = 2a + 2\pi k$ with $k \in \mathbb{N}^+$. It is interesting to note that this interval can be shorted to one half of the period, if $\cos(2a)$ is zero. By exploiting this feature of the trigonometric functions, the individual model coefficients are calculated by multiplying the sine or the cosine to the measured data $s(t)$ and integrating over all times as shown by Cohen (1995, Chap. 15):

$$a_k = \frac{2}{T} \int_{-\infty}^{\infty} s(t) \cos(\omega_k t) dt \quad (7)$$

$$b_k = \frac{2}{T} \int_{-\infty}^{\infty} s(t) \sin(\omega_k t) dt. \quad (8)$$

For a measured signal, the integration can only be performed over the interval $[0, T]$. It is obvious that an error is introduced, if $T \neq 2\pi n$. In order to investigate the properties of the finite integration, we will concentrate in the following on the cosine term (Eq. (7)), since the analysis of the sine term (Eq. (8)) is similar. By setting the integral boundaries to the finite time interval the integral in Eq. (7) can be written as

$$\int_0^T s(t) \cos(\omega_k t) dt = \int_0^T \left(a_k \cos^2(\omega_k t) + b_k \sin(\omega_k t) \cos(\omega_k t) + \epsilon_k(t) \cos(\omega_k t) \right) dt. \quad (9)$$

With the two identities $\cos^2(x) = \frac{1}{2}(1 + \cos(2x))$ and $\sin(x) \cos(x) = \frac{1}{2} \sin(2x)$ the integral (9) is then expanded to

$$\begin{aligned} & \int_0^T s(t) \cos(\omega_k t) dt \\ &= \frac{a_k}{2} \int_0^T \left(1 + \cos(2\omega_k t) + 2 \frac{b_k}{a_k} \sin(2\omega_k t) \cos(\omega_k t) \right) dt \\ & \quad + \int_0^T \epsilon_k(t) \cos(\omega_k t) dt \quad (10) \end{aligned}$$

and further reduced to

$$\begin{aligned} & \frac{2}{T} \int_0^T s(t) \cos(\omega_k t) dt \\ &= a_k \left(1 + \underbrace{\frac{1}{T} \int_0^T \left(\cos(2\omega_k t) + \frac{b_k}{a_k} \sin(2\omega_k t) \right) dt}_{\text{truncation error } \epsilon_{\text{Tk}}} \right) \\ & \quad + \underbrace{\frac{2}{T} \int_0^T \epsilon_k(t) \cos(\omega_k t) dt}_{\text{random error } \epsilon_{\text{FSk}}}. \quad (11) \end{aligned}$$

The equation above indicates that the coefficient a_k is effected by two errors ϵ_{Tk} (truncation) and ϵ_{FSk} (random) which might be nonzero for an arbitrary T . Thus, if both errors are neglected, the integral on the left hand side turns into an approximation of a_k . Taking the consideration about the orthogonality described in Eq. (5) into account, ϵ_{Tk} becomes only zero, if the integration time T is an integer multiple of π/ω_k . This means for the Fourier series that a given integration time T (observation window) defines the lowest allowed frequency ω_0 . Furthermore, only multiples of this fundamental frequency $\omega_k = k\omega_0$ with $k \in \mathbb{N}$ are allowed in the Fourier series because $\epsilon_{\text{Tk}} = 0$ in this case.

The technical realization of OMD is called quadrature demodulation, which is the discrete version of equation (11) by replacing the integral over $s(t)$ into a sum over the discrete sampled values $\hat{s}_n, 0 \leq n \leq N-1$ and setting the truncation error to zero. For a time discrete signal with N samples and equidistant sampling with a constant sampling period T_s , and $t_n = nT_s$, the parameter a_k is approximated for a certain frequency ω_k by

$$a_k \approx \frac{2}{N} \sum_{n=0}^{N-1} \hat{s}_n \cos(\omega_k t_n). \quad (12)$$

According to the previous considerations, the truncation error ϵ_{Tk} is larger than zero, if the measurement range $T = NT_s$ is not exactly a multiple of π/ω_k as shown in Figure (1). In this example a signal with a time period of $t = 2\pi$ is sampled with $N = 23$, $T_s = 2\pi/20$. The total integration time is $T = 2\pi + 1/5\pi$, being slightly longer than the period of the signal, which is indicated by the two additional sampling points after $t = 2\pi$. The truncation error equals the gray shaded area.

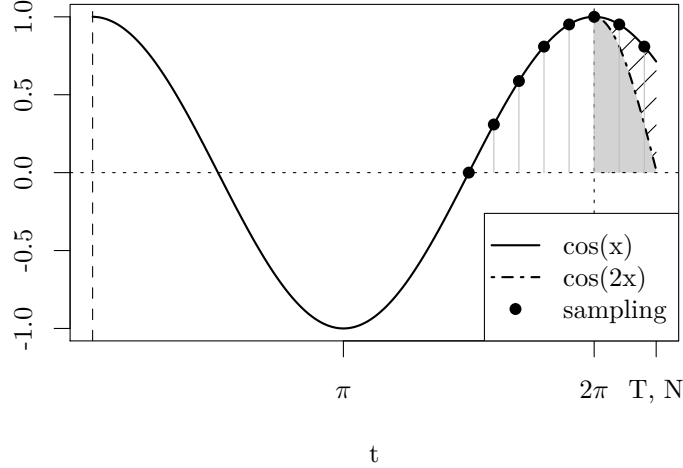


Figure 1: Example of the truncation error of a signal with the time period of 2π , which is generated by the last two samples and the value is indicated by the gray shaded area.

Generally speaking, the sampling error in the discrete T_s version can be estimated by

$$\frac{2}{N} \sum_{n=0}^{N-1} \hat{s}_n \cos(\omega_k t_n) \approx a_k \underbrace{\left(1 + \frac{\Delta\varphi}{T}\right)}_{\epsilon_{Tk}} \pm \underbrace{\Phi_{1-\alpha} \frac{2\sigma}{\sqrt{N}}}_{\epsilon_{FSk}}, \quad (13)$$

where $\Delta\varphi = \min(T - \pi i/\omega_k)$ with the according $i \in \mathbb{N}$ and the random error is modeled by the α -quantile of the sampling error distribution $\Phi_{1-\alpha}$ related to the underlying process with its standard deviation σ . This estimates the confidence interval of a_k and b_k respectively.

The above considerations lead to following four statements, which are derived in detail in the appendix: (i) the maximum absolute value of the truncation error is bounded from above by $|\epsilon_{Tk}| \leq 0.2$ which is reached, if $T \gtrsim \pi/\omega_k$, which is consistent with the experimental findings from Thompson & Tree (1980); (ii) ϵ_{Tk} is independent from total number of samples N for a constant time T , which makes the OMD a non-consistent estimator for model parameters a_k and b_k ; (iii) by increasing the sample rate the measurement error decreases by $\mathcal{O}(N^{-0.5})$, but scales with twice the standard deviation of noise distribution; (iv) DFT can be derived from equation (13) by restricting to equidistant sampling with constant

Concluding, the truncation error, which is an intrinsic feature of OMD, produces a systematic deviation from the true value depending on the difference between the sampling time interval and the corresponding period of the frequency of interest. In contrast to that, the random error diminishes with increasing sampling rate $T_s^{-1} = N/T$. A detailed discussion on this topic can be found in Jerri (1977); Shannon (1949); Thompson & Tree (1980). In case of multivariate and randomly sampled data the recent work of Al-Ani & Tarczynski (2012) suggests two calculation schemes estimating the Fourier transform in the general case. The continuous time Fourier transform estimation (similar to Eq. (12)) takes samples with arbitrary spacing as the general approach, in contrast to the secondly proposed discrete time Fourier transform ($t_n = nT_s$ and $\omega_k = k\omega_0$) estimation scheme. Here the data is projected onto a regular grid, which now may provide locations of missing data. Both schemes consider the sampling pattern t_n and its power spectrum distribution function $p(t_n)$. However, even for such sophisticated methods, the main conceptual drawbacks (see points (i) and (ii)) remain, which motivates the subsequent Lomb-Scargle method as non OMD method and its extension to multivariate data.

2.3 Approach iii – Lomb Scargle method

As described in the previous section, the disadvantage of OMD is that cosine and sine are not orthogonal on arbitrary intervals. By introducing an additional parameter $\tau \in \mathbb{R}$ into Equation (5) it will be shown that

$$\int_a^b \cos(x - \tau) \sin(x - \tau) dx = 0 \quad (14)$$

holds for arbitrary intervals $[a, b]$. By utilizing the trigonometric identities, $\cos^2(\phi) - \sin^2(\phi) = \cos(2\phi)$ and $\cos(\phi) \sin(\phi) = \frac{1}{2} \sin(2\phi)$, to remove the differences in the arguments the integral can be transformed to

$$\int_a^b \left(\frac{1}{2} \sin(2x) \cos(2\tau) - \frac{1}{2} \sin(2\tau) \cos(2x) \right) dx = 0.$$

If this integral has to be zero, the following condition has to hold

$$\cos(2\tau) \int_a^b \sin(2x) dx = \sin(2\tau) \int_a^b \cos(2x) dx$$

which can be transformed to

$$\frac{\int_a^b \sin(2x) dx}{\int_a^b \cos(2x) dx} = \tan(2\tau). \quad (15)$$

Therefore, equation (15) calculates the parameter τ in such a way that expression (14) is zero again. In case of equidistant sampling, the value of τ can be directly calculated from the integration boundaries in the following way:

$$\tau = \frac{b - a}{2}.$$

Based on this general consideration the time shifting parameter $\tau_k \in \mathbb{R}$, $0 \leq k \leq M$, was introduced by Lomb and Scargle for frequency ω_k into the model given in Equation (2)

$$s(t) = \sum_{k=0}^M (a_k \cos(\omega_k(t - \tau_k)) + b_k \sin(\omega_k(t - \tau_k)) + \epsilon_k(t)) \quad (16)$$

in order to remove the truncation error. The parameter τ_k can be calculated by

$$\tan(2\omega_k \tau_k) = \frac{\int_a^b \sin(2\omega_k t) dt}{\int_a^b \cos(2\omega_k t) dt} \quad (17)$$

similar to equation (15). For the time discrete version the integrals transform into a sum resulting in

$$\tan(2\omega_k \tau_k) = \frac{\sum_{n=0}^{N-1} \sin(2\omega_k t_n)}{\sum_{n=0}^{N-1} \cos(2\omega_k t_n)}. \quad (18)$$

The parameters a_k and b_k can be determined beginning with Equation (10) but factorize it by $\cos^2 x$, instead of expanding $\cos^2 x$ to $\frac{1}{2}(1 + \cos(2x))$ as done in Equation (11). Since the method is applied to sampled data, the method will be delineated for the discrete set \hat{s}_i in the following. The data is multiplied by $\cos(\omega_k(t_n - \tau_k))$ resulting in the next equation for a single frequency ω_k with $\phi_k = \omega_k(t_n - \tau_k)$ as a substitution:

$$\begin{aligned} \sum_{n=0}^{N-1} \hat{s}_n \cos(\phi_k) &= a_k \sum_{n=0}^{N-1} \cos^2(\phi_k) + b_k \underbrace{\sum_{n=0}^{N-1} \sin(\phi_k) \cos(\phi_k)}_{\text{truncation error } \epsilon_{\text{Tk}}} \\ &+ \underbrace{\sum_{n=0}^{N-1} \epsilon_k(t_n) \cos(\phi_k)}_{\text{modulated error } \epsilon_{\text{LSk}}}. \quad (19) \end{aligned}$$

The sum over the term $\cos(x) \sin(x)$ vanishes because of the proper selection of τ_k according to Equation (18). The sum over $\epsilon_k(t_n) \cos(\phi_k)$ describes the modulated noise distribution function. The sum over $\cos^2(\phi_k)$ is the dominating term to calculate the value of parameter a_k which can be directly obtained by dividing by $\sum_{n=0}^{N-1} \cos^2(\phi_k)$, which gives

$$\frac{\sum_{n=0}^{N-1} \hat{s}_n \cos(\phi_k)}{\sum_{n=0}^{N-1} \cos^2(\phi_k)} = a_k + \underbrace{\frac{\sum_{n=0}^{N-1} \epsilon_k(t_n) \cos(\phi_k)}{\sum_{n=0}^{N-1} \cos^2(\phi_k)}}_{\epsilon_{\text{LSk}}}. \quad (20)$$

The residual error term on the right hand side consists of a random distributed part divided by a sum over the square of the cosine. In contrast to OMD, the estimation error of the parameter a_k only depends on noise and is independent from the realization of sampling.

The next step is to determine ϵ_{LSk} in terms of a confidence interval with respect to α as it was done for OMD

in Equation (13). Given a normal distributed error function $\epsilon_k \leftrightarrow \mathcal{N}(0, \sigma)$, with expectation value of zero and standard deviation σ independent from time, the error can be factorized (Parzen (1962, Theorem 4A, p. 90)), leading to

$$\epsilon_{\text{LS}} = \Phi_{1-\alpha} \frac{\sigma}{\sqrt{N}} \frac{\sum_{n=0}^{N-1} \cos(\phi)}{\underbrace{\sum_{n=0}^{N-1} \cos^2(\phi)}_{e_{\text{max}}}} \quad (21)$$

estimating the most probable limits of ϵ_{LS} . Here $\Phi_{1-\alpha}$ denotes the α -quantil of the given distribution function. Since the estimation error neither depend on the frequency nor the shifting parameter, we estimate

$$e_{\text{max}} = \max_{\beta} \left[\frac{\int_0^{\beta} \cos(\phi) d\phi}{\int_0^{\beta} \cos^2(\phi) d\phi} \right]. \quad (22)$$

Without loss of generality we set $\omega_k = 1$ and $\tau_k = 0$. In order to maximize e_{max} for $\beta \in [0, 2\pi]$, Equation (22) must be integrated which results $4 \sin(\beta)/(2\beta + \sin(2\beta))$ so that the maximum error is $e_{\text{max}} = \frac{4}{\pi}$ for $\beta = \pi/2$. The final parameter estimation gives

$$a_k = \frac{\sum_{n=0}^{N-1} \hat{s}_n \cos(\omega_k(t_n - \tau_k))}{\sum_{n=0}^{N-1} \cos^2(\omega_k(t_n - \tau_k))} \pm \underbrace{\frac{4}{\pi} \Phi_{1-\alpha} \frac{\sigma}{\sqrt{N}}}_{\Delta a_k = \Delta b_k}, \quad (23)$$

where the error converges to zero by increasing the number of samples N for a fixed time interval. This property qualifies LSM to be a consistent estimator in amplitude and phase (Mathias et al. 2004), because by increasing the number of samples the estimation gets more precise.

In comparison to the classical definition of Lomb (1976) the coefficients a_k and b_k differ by a factor of $\sqrt{N/2}$ scaling the result. With a closer look to the original equations

$$a_{k,\text{orig}} = \frac{\sum_n \hat{s}_n \cos(\omega_k(t_n - \tau_k))}{\sqrt{\frac{N}{2}} \sqrt{\sum_n \cos^2(\omega_k(t_n - \tau_k))}}$$

this factor becomes evident, e. g. Hocke (1998). Since $\lim_{n \rightarrow \infty} \sum_n \cos^2(\omega_k(t_n - \tau_k)) \approx N/2$ can be assumed, $a_k \approx a_{k,\text{orig}}$ is valid, if N fits exactly to a multiple of ω_k . Because the presented approach is related to the rather

technical amplitude demodulation procedure, we assume equation (23) to be more accurate.

The confidence interval Δa_k for parameter a_k can be approximated by

$$\Delta a_k = \frac{4}{\pi} \Phi_{1-\alpha} \frac{\sigma}{\sqrt{N}},$$

which is smaller than the value for OMD given in Equation (13). The confidence interval for the amplitude ΔA_k can be deduced by propagating the error

$$\begin{aligned} \Delta A_k &= \frac{\partial A_k}{\partial a} \Delta a_k + \frac{\partial A_k}{\partial b} \Delta b_k \\ &= \frac{4}{\pi} \Phi_{1-\alpha} \sqrt{\frac{2}{N}} \sigma. \end{aligned} \quad (24)$$

In a similar way, the confidence interval for the phase φ_k can be defined by

$$\begin{aligned} \varphi_k &= \tan^{-1} \left(\frac{b_k}{a_k} \right) \pm \Delta \varphi \\ &= \tan^{-1} \left(\frac{b_k}{a_k} \right) \pm \frac{4}{\pi} \Phi_{1-\alpha} \sqrt{\frac{2}{N}} \frac{\sigma}{A_k}. \end{aligned} \quad (25)$$

It is interesting to note that the confidence interval for the phase φ_k decreases when the amplitude is increasing.

In order to determine the spectrum with LSM, we assume the recorded signal is described by many frequencies. The most significant frequency is then represented by a peak in the frequency spectrum of a certain width and height. The width is determined by the frequency resolution Δf which equals $1/T$. From this point of view the precision of a frequency estimation changes only with observation length T and seams to be independent from the number of samples N and signal quality. The quality Σ is measured by a signal-to-noise ratio like expression

$$\Sigma = \sqrt{\frac{1}{N} \sum_{n=0}^{N-1} \frac{(s_n - y_n)^2}{\sigma_n^2}} \approx \frac{\sqrt{\sum_l A_l^2}}{\sqrt{\frac{1}{N} \sum_{n=0}^{N-1} (\epsilon(t_n))^2}} \quad (26)$$

with A_l counting the *significant* amplitudes. Here y_n denotes the fitted model and σ_n the uncertainty per sample, which is related to σ by $\sigma = \sqrt{\frac{1}{N} \sum_{n=0}^{N-1} \sigma_n^2}$ and $\epsilon(t_n)$ as the noise per sample. Following VanderPlas (2017) we apply Bayesian statistics and assume that every

peak is Gaussian shaped, i. e. $e^{P(f_{\max} \pm \Delta f)} \propto e^{-\Delta f^2 / (2\sigma_f^2)}$. It follows that a significant peak $A_{\max}^2 = A^2(f_{\max})$ appears at f_{\max} , in a way that $A_{\max}^2/2 = A^2(f_{\max} \pm \Delta f)$ is valid. Here, A^2 is related to the power spectral density $P(f) \propto a_k^2 + b_k^2$. The frequency uncertainty (or standard deviation) is then given by

$$\sigma_f \approx \Delta f \sqrt{\frac{2}{N\Sigma^2}}$$

so that a significant peak is located in the interval $f_{\max} \pm \sigma_f$. This approach suggests that increasing the number of samples in a fixed interval T enhances the precision of f_{\max} by reducing σ_f . However, if the original signal contains two frequencies with a distance in the range of $1/T$, it cannot be excluded even for LSM that these peaks merge together in one single peak with small σ_f according to Kovács (1981).

Concluding the properties of LSM: (i) there is no truncation error $\epsilon_T = 0$; (ii) LSM provides a better noise rejection compared to OMD, $\epsilon_{LS} < \epsilon_{FS}$; (iii) the explicit sampling pattern is not of interest to work with LSM.

2.4 Power Spectral Density and False Alarm Probability

In this work the simplest case of uncorrelated and mean free Gaussian noise is assumed which suits many common technical and scientific cases. From the power spectral density (PSD) $P_k = \frac{N}{4\sigma_0^2}(a_k^2 + b_k^2)$, with $\sigma_0^2 = \sum_{n=0}^{N-1} (y(t_n) - \bar{y})^2$ as the variance of the sample, refer to Hocke (1998) and Zechmeister & Kürster (2009), the standardized PSD is defined by

$$\text{psd}(\omega_k) = P_k p_k \quad (27)$$

on the interval $[0, 1]$, where p_k is the standardized Gaussian noise. Here, P_k is similar to a signal to noise ratio given in Equation 26 (see Scargle (1982)). Since LSM calculates the result of a least square fit, a value of $\text{psd}(\omega_k) = 1$ indicates a “perfect” fit to the corresponding model function. In the case of $\text{psd}(\omega_k) = 0$ no correspondence is visible. The discussion about the presented standardization is carried out in detail by Cumming et al. (1999). The different ways to perform the calculation of the psd-value are briefly summarized in Zechmeister & Kürster (2009). Additionally, a more precise description

of noise takes some effort which should be accomplished by analyzing the measurement data or by taking additional noise measurements. The different procedures are briefly described by Cumming et al. (1999) and Horne & Baliunas (1986).

The standardized noise level reads $p_k = 2/(N - 1)$, so the standardized power spectral density

$$\text{psd}(\omega_k) = \frac{N}{N - 1} \frac{A_k^2(\omega_k)}{2\sigma_0^2} \quad (28)$$

can be calculated directly from the power spectral density or amplitude. A more sophisticated approach relies on a Bayesian estimate of $\text{psd}(\omega_k)$ which is presented in Mortier et al. (2015). For most technical applications equation (28) should be sufficient.

As a statistical measure, the probability

$$\mathcal{P}(P_k > P_0) = (1 - \text{psd}(\omega_k))^{\frac{N-3}{2}} \quad (29)$$

states that there is no PSD peak P_k larger than a reference value P_0 of the best fit. From here the statistical significance of a single frequency ω_k can be deduced as the so called false alarm probability (FAP) with

$$\text{FAP} = \begin{cases} 1 - (1 - \mathcal{P}(P_k > P_0))^M & , \text{ if } \mathcal{P}(P_k > P_0) \approx 1 \\ M\mathcal{P}(P_k > P_0) & , \text{ if } \mathcal{P}(P_k > P_0) \ll 1 \end{cases} \quad (30)$$

where M denotes the number of independent (fundamental) frequencies present in the signal. The discussion about this degree of freedom is very diverse in literature and is discussed for instance by VanderPlas (2017). The first approach is Shannon’s sampling theorem as a pragmatic and conservative access to this topic. It states that the number of independent frequencies is $M \approx N/2$. At the same moment a band limited signal is required which is sampled with twice the maximum signal frequency $f_s \geq 2 \max(f)$. It follows that signal frequencies above $f_s/2$ become visible as an alias in the lower frequency domain. In this aspect randomly sampled data may behave different. For randomly sampled data the conservative approach defines an average sampling rate $\bar{f}_s = N/T$ which will lead to $M \approx T\bar{f}_s/2$ as a lower limit. The parameter T scales the total sampling (e. g. time) range interval in one dimension. However, the question about the possible maximum frequency which can be detected in randomly sampled data, still remains. If

we assume sampling points originating from a regular grid, but with randomly distributed missing values, then $f_s \approx \min(\Delta t)^{-1}$ relates to the minimal distance between two neighboring points as upper limit of f_s . Data in such a grid is taken at $t_i = t_1 + n_i p$ instances, where p is a kind of a common divisor, refer to Eyer & Bartholdi (1999) and n_i is a non complete set of values to reach every location. Given $n_i \in \mathbb{N}^+$ we will find that the effective maximum frequency fulfills $f_s > \overline{f_s}$. Care must be taken with this assumption, because it could lead to undesired large values of f_s and therefore wrong estimations of M .

Horne & Baliunas (1986) carried out an extensive study about the number of independent frequencies (and the maximum detectable frequency). They found an empirical approximation

$$M = -6.362 + 1.193N + 0.00098N^2, \quad (31)$$

which is a compromise between the conservative $N/2$ and the artificially large minimal distance value. A detailed discussion on FAP and the independent frequencies can be found in the studies by Baluev (2008, 2013b,a).

3 The multivariate Lomb-Scargle method

A signal S depending of n -independent variables represents a function $\mathbb{R}^m \rightarrow \mathbb{R}$ with the input vector described by $\vec{t} = [t_1, t_2, \dots, t_m]$. The model function for multivariate LSM is gained by replacing the arguments of cosine and sine in the univariate model function in Equation (16) by vectors resulting in

$$Y(\vec{t}) = \sum_{k=0}^M (a_k \cos(\vec{\omega}_k \cdot (\vec{t} - \vec{\tau}_k)) + b_k \sin(\vec{\omega}_k \cdot (\vec{t} - \vec{\tau}_k))). \quad (32)$$

In this case, the shifting parameter $\vec{\tau}_k \in \mathbb{R}^m, 0 \leq k \leq M$, is a vector and in principle hard to calculate. However, if the argument of the cosine is expanded, it is obvious that the scalar product $\vec{\omega}_k \cdot \vec{\tau}_k \in \mathbb{R}$ does not depend on time and thus, the cosine argument can be written as $\vec{\omega}_k \cdot \vec{t} - \tau_k^*$ with $\tau_k^* = \vec{\omega}_k \cdot \vec{\tau}_k$. The determination of τ_k^* is similar as for τ shown in Equation (17), but with some differences in the equations since the phase, instead of the time coordinate, is shifted now. This is shown in the following.

3.1 Derivation of the shifting parameter

In this section it is shown that shifting the phase, instead of time, does not affect the Lomb-Scargle algorithm. The derivation of the shifting parameter for the multivariate case is delineated for the time discrete signal $\hat{S} = \{(\hat{S}_i, \vec{t}_i) \in \mathbb{R}^{m+1}, 0 \leq i \leq N-1\}$. Starting with the orthogonality condition

$$\sum_n \sin(\vec{\omega}_k \cdot \vec{t}_n - \tau_k^*) \cos(\vec{\omega}_k \cdot \vec{t}_n - \tau_k^*) = 0 \quad (33)$$

and applying the trigonometric identities to remove the differences in the arguments:

$$\sum_n \left[\left(\underbrace{\cos(\vec{\omega}_k \cdot \vec{t}_n)}_{cs} \underbrace{\cos(\tau_k^*)}_{ct} + \underbrace{\sin(\vec{\omega}_k \cdot \vec{t}_n)}_{ss} \underbrace{\sin(\tau_k^*)}_{st} \right) \right. \\ \left. \left(\underbrace{\sin(\vec{\omega}_k \cdot \vec{t}_n)}_{ss} \underbrace{\cos(\tau_k^*)}_{ct} - \underbrace{\cos(\vec{\omega}_k \cdot \vec{t}_n)}_{cs} \underbrace{\sin(\tau_k^*)}_{st} \right) \right] = 0 \quad (34)$$

By using the defined abbreviations this equation can be simplified to

$$\sum_n (cs \, ss \, ct^2 + ss^2 \, st \, ct - cs^2 \, ct \, st - ss \, cs \, st^2) = 0.$$

After rearranging the summation (the terms ct and st do not depend on n) the following equation is deduced:

$$\sum_n (cs^2 \, ct \, st - ct \, st \, ss^2) = \sum_n (cs \, ss \, ct^2 - ss \, cs \, st^2) \\ \sum_n ct \, st (cs^2 - ss^2) = \sum_n cs \, ss (ct^2 - st^2) \\ \frac{ct \, st}{ct^2 - st^2} = \frac{\sum_n cs \, ss}{\sum_n (cs^2 - ss^2)} \quad (35)$$

The fraction on both sides can be simplified by applying $\cos^2(x) - \sin^2(x) = \cos(2x)$ and $\cos(x) \sin(x) = \frac{1}{2} \sin(2x)$ resulting in

$$\frac{\frac{1}{2} \sin(2\tau^*)}{\cos(2\tau^*)} = \frac{\frac{1}{2} \sum_{n=0}^{N-1} \sin(2\vec{\omega}_k \cdot \vec{t}_n)}{\sum_{n=0}^{N-1} \cos(2\vec{\omega}_k \cdot \vec{t}_n)},$$

and then the fraction on the left hand side is replaced by the tangent

$$\tan(2\tau^*) = \frac{\sum_{n=0}^{N-1} \sin(2\vec{\omega}_k \cdot \vec{t}_n)}{\sum_{n=0}^{N-1} \cos(2\vec{\omega}_k \cdot \vec{t}_n)}. \quad (36)$$

In comparison with one dimensional LSM, the frequency ω_k is missing on the left side in Equation (36).

3.2 Parameter estimation

Similar to the procedure for the LSM for a discrete signal in one dimension (see Equation (19)), a discrete multivariate signal (\hat{S}_i, \vec{t}_i) with N samples is multiplied by $\cos(\vec{\omega}_k \cdot \vec{t}_i - \tau_k^*)$ resulting in

$$\sum_n \hat{S}(\vec{t}_n) \cos(\vec{\omega}_k \cdot \vec{t}_n - \tau_k^*) = \sum_{n=0}^{N-1} \left(a_k \cos^2(\vec{\omega}_k \cdot \vec{t}_n - \tau_k^*) + \underbrace{b_k \sin(\vec{\omega}_k \cdot \vec{t}_n - \tau_k^*) \cos(\vec{\omega}_k \cdot \vec{t}_n - \tau_k^*)}_{=0, \text{if orthogonal}} \right).$$

The determination of the parameter a_k is similar to the one-dimensional case shown in Equation (20):

$$\frac{\sum_{n=0}^{N-1} y(\vec{t}_n) \cos(\vec{\omega}_k \cdot \vec{t}_n - \tau_k^*)}{\sum_{n=0}^{N-1} \cos^2(\vec{\omega}_k \cdot \vec{t}_n - \tau_k^*)} = a_k. \quad (37)$$

The parameter b_k is calculated analogously:

$$\frac{\sum_{n=0}^{N-1} y(\vec{t}_n) \sin(\vec{\omega}_k \cdot \vec{t}_n - \tau_k^*)}{\sum_{n=0}^{N-1} \sin^2(\vec{\omega}_k \cdot \vec{t}_n - \tau_k^*)} = b_k. \quad (38)$$

The power spectral density (Eq. (28)) as well as the false alarm probability (Eq. (30)) are calculated in the same way compared to the method in section 2.4.

4 Application

The applications are ordered by the complexity of the sampling. Starting with a regular grid with missing values for the synthetic test data, the measurements of the ultrasound Doppler velocimetry contains jitter and missing values. The most general scenario is then given by the astrophysical 2D data set of sunspots, which appear freely in time and space.

An implementation of the multivariate Lomb-Scargle method is available in the `spectral` package published on CRAN (Seilmayer 2019) to give the user access to a multi-dimensional analysis with an easy to use interface.

4.1 Synthetic Test Data

Let's start with a simple test case, where the input signal is a simple two dimensional plain wave

$$z = \cos\left(2\pi(f_x x + f_y y) + \frac{\pi}{4}\right)$$

with $f_x = 3.25$ and $f_y = 6.32$ as the dimensionless frequencies, which are specifically selected in such a way that $f_x, f_y \neq k \cdot \omega_0$. Furthermore, data gaps are modeled by removing randomly distributed and uncorrelated grid points covering 60% of the total data set. As LSM requires an appropriate input vector of frequencies we choose for both variables $f_x, f_y \in [-10, 10]$ with a resolution of $\delta f_x, \delta f_y = 0.025$. Figure 2a shows the nonuniform distributed input data in the range of $x, y \in [-1, 1]$ with $\delta x, \delta y = 0.025$. With respect to the chosen frequencies f_x and f_y it becomes evident, that both frequency parts do not fit to the data range by an integer fraction. Gray areas indicate missing (non available numbers “nan”) values.

The corresponding power spectral density shown in Figure 2b displays the maxima at the 1st and 3rd quadrant, which represents a wave traveling upwards. The figure illustrates that even with a huge amount of missing data it is possible to properly detect the periodic signal. In the present case the value of $\text{psd}(f_x, f_y) \approx 1$ indicates a perfect fit to the corresponding sinusoidal model. For comparison Figure 2c depicts the standardized PSD (compare with Eq. 28)

$$\text{psd}_{\text{FT}}(\vec{\omega}) = \frac{N}{N-1} \cdot \frac{1}{2\sigma_0^2} \left(\frac{2|\mathcal{F}(z(x, y))|}{1 - \frac{N_{\text{Zero}}}{N}} \right)^2 \quad (39)$$

calculated from a discrete Fourier transform symbolized by the operator $\mathcal{F}(g(x))(\omega) = \int g(x) e^{i\omega x} dx$. Here missing values (nan) are handled by zero padding which means that the introduced gaps are filled with 0. Because Fourier transform represents a conservative transformation (mapping) into the spectral domain, zero padding lead to a significant reduction of the average signal energy. A proper rescaling to the number of zeros N_{Zero} (missing

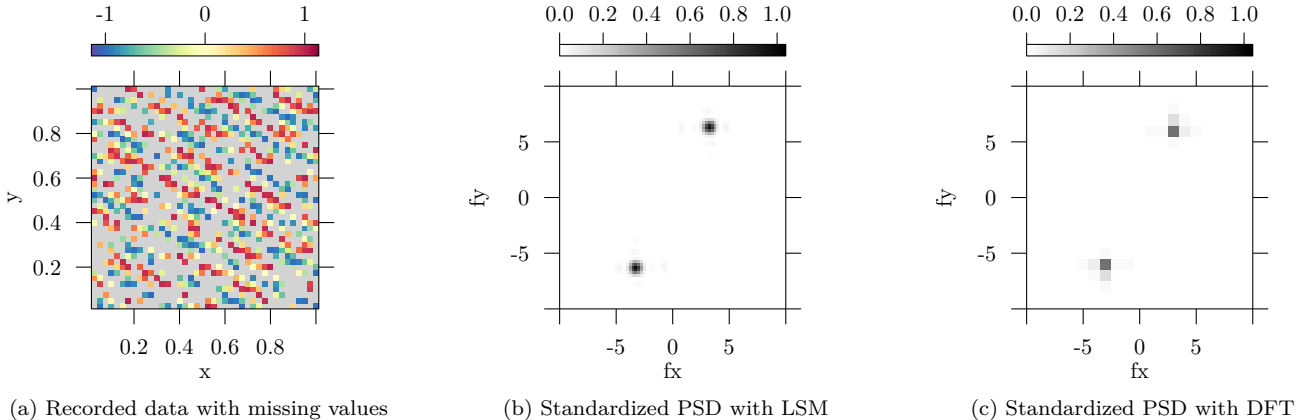


Figure 2: Comparison of the power spectral density PSD calculated with the LSM and with the DFT approach for a two-dimensional input data with missing values. (a) Sampled data $z = \cos(2\pi(xf_x + yf_y) + \pi/4)$ for $x, y \in [-1, 1]$ with $\delta x, \delta y = 0.025$ and $f_x = 3.25$ and $f_y = 6.32$. Gray areas represent missing values. (b) PSD calculated with the LSM and (c) PSD calculated with DFT. Notice that the systematic error ϵ_T and the sparse resolution leads to a rough approximation of the frequency and to a reduced amplitude (by 50%) in the PSD calculated by DFT.

values) is required to ensure approximated amplitude estimations. Zero padding always changes the character of the input signal in a way that the corresponding DFT treats the zeros as if they were part of the original signal. The resulting PSD becomes finally different from the original one.

Since the signal frequencies $f_x, f_y \neq k/T_{x,y}$ do not fit into an integer spaced scheme ($k \in \mathbb{N}$) of the data range $T_{x,y} = 2$, the discrete Fourier transform suffers from its drawbacks, which were briefly discussed before. The effect of leakage and misfit of frequencies can be recognized in Figure 2c in terms of a rather coarse resolution and a lower PSD value.

4.2 3D UDV Flow Measurement

The second example is taken from previous experimental flow measurements from Seilmayer et al. (2014) for the magneto rotational instability Seilmayer et al. (2014). The experiment consists of a cylindrical annulus containing a liquid metal between the inner and the outer wall. In this experiment the inner wall is rotating at a frequency $\omega_{\text{in}} = 2\pi \cdot 0.05 \text{ Hz}$ and the outer wall at a frequency $\omega_{\text{out}} = 2\pi \cdot 0.013 \text{ Hz}$. The flow is driven by shear since

$\omega_{\text{in}} - \omega_{\text{out}} > 0$. Two ultrasound sensors mounted at the outer cylinder, on opposite side of each other, measure the axial velocity component v_z along the line of sight parallel to the rotation axis of the cylinder. Additionally, the liquid metal flow is exposed to a magnetic field $B_\varphi \propto r^{-1}$ originating from a current I_{axis} on the axis of the cylinder. A typical time series of the axial velocity (along the measuring line) is displayed in the Figure 3. The existence of periodic patterns in this figure indicates a traveling wave propagating in the fluid. In cylindrical geometry the traveling wave can be expressed as

$$v_z(t, r, z, \varphi) \propto v_0(r) e^{i(\omega t + kz + m\varphi)}, \quad (40)$$

with $\omega = 2\pi f$ as the corresponding drift frequency, k as the vertical spatial structure and m as the azimuthal symmetry. A closer look to the picture indicates that this wave is not axial symmetric with $m = 1$ which is proven with data analysis in the following.

The preparation of data requires a mapping

$$v_z := f(t_n, d_n, \varphi_{1,n}, \varphi_{2,n}) \quad (41)$$

with

$$\varphi_{1,n} = \omega_{\text{out}} t_n \text{ (sensor 1, S1)} \quad (42)$$

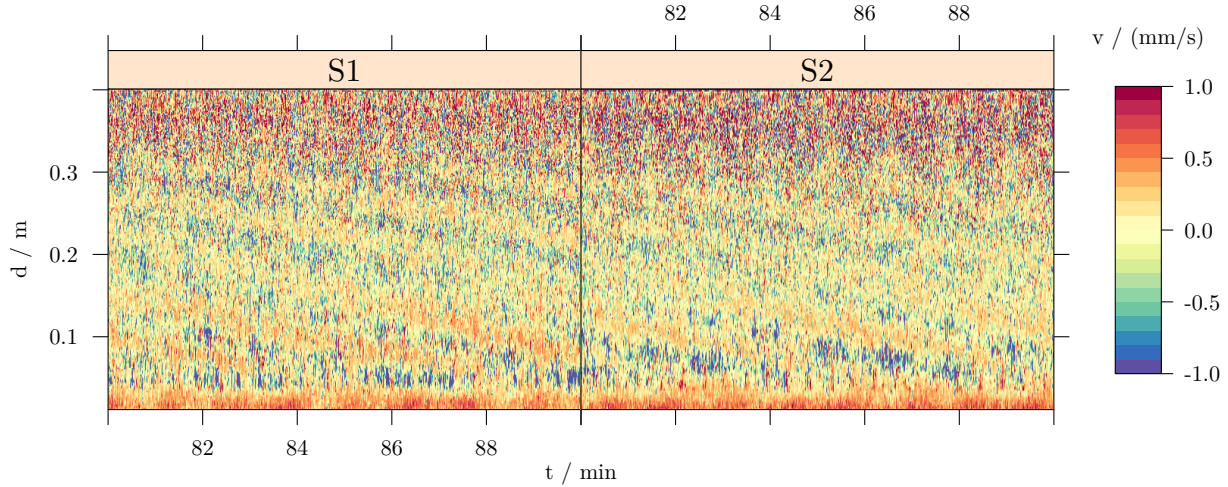


Figure 3: Sensor data in the co-rotating reference frame. Data is taken as time series from two rotating sensors. The measurement time of the sensor data is folded with its individual phase location, so $\varphi_{S1} = \omega t$ and $\varphi_{S2} = \omega t + \pi$ describe the two ordinates.

and

$$\varphi_{2,n} = \omega_{\text{out}} t_n + \pi \text{ (sensor 2, S2)} \quad (43)$$

with the azimuthal angles $\varphi_{2,n} = \varphi_{1,n} + \pi$ depending on time as the sensors are attached to the outer wall. The subscript n indicates the sampling in this sense. Finally, the measured time series v_z depends on time t_n , depth d_n and angular position φ_n . This fits perfectly to the proposed multivariate LSM.

Figure 4 illustrates the result of the LSM decomposition into several m -modes showing the amplitudes. The $m = 0$ mode contains a stationary structure at $f \approx 0$, which originates from sensor miss-alignments and (thermal) side effects in the flow. The minor non-stationary components, here the two point-symmetric peaks, originate from cross-talk (or alias projections) of the $m = 1$ mode for two reasons: (i) because the sensors behave not exactly identical (e. g. misalignment or different sensitivity) and therefore respond slightly different to the same flow signal. This means that one of the sensors projects a little bit more energy into the data than the other. This leads to a “leakage”-effect and a weak signal in $m = 0$ mode. (ii) the outer rotation of the sensors acts like an additional sampling frequency f_{out} . In consequence, the spectrum of this regular sampling function folds with the

spectrum of the observed process leading to alias images (copies) of the original process spectrum into other frequency ranges (i. e. m 's). That is why the non stationary and point-symmetric (with reference to the origin) signals in the $m = 0$ panel correspond to the (mirrored) patterns originally present in the $m = 1$ panel.

The AMRI wave itself is located in the $m = 1$ panel with a characteristic frequency in time (f) and space (k). Here, two components can be identified: the dominant wave at $f \approx 9$ mHz and $k \approx 20 \text{ m}^{-1}$ and a minor counterpart at $f \approx 4$ mHz and $k \approx -20 \text{ m}^{-1}$. The signals in $m = 3$ and $m = 5$ might be assigned to aliases from the inner rotation $f_i = 0.05$ Hz.

The advantage of “high” dimensional spectral decomposition is the improved noise rejection. With respect to the raw data given in Figure 3 it is obvious that high frequency noise is present in the data. Depending on the exact distribution of noise its energies spread over a certain range of frequencies. If we would select a representative depth and angle so that $d_n, \varphi_n = \text{const.}$, the velocity v_z only depends on time. In the subsequent one dimensional analysis the noise would accumulate along the single frequency ordinate probably hiding the signal of interest. Taking the higher order analysis distributes

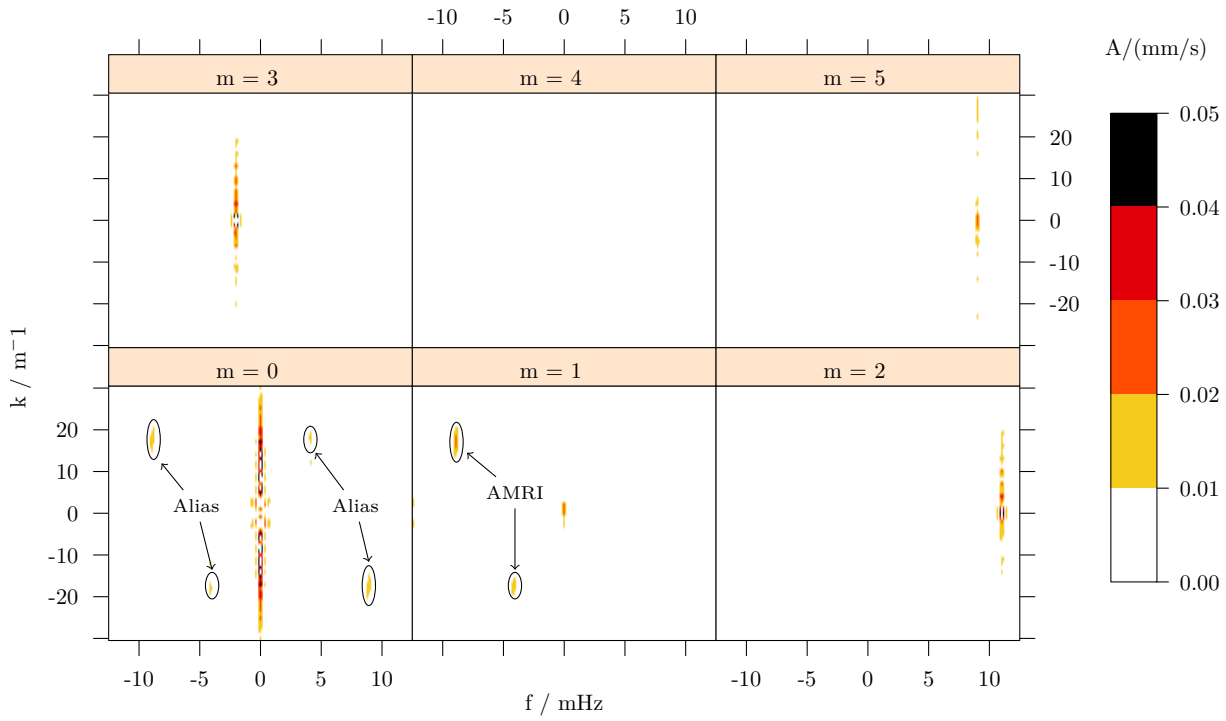


Figure 4: Spectrum of sensor data. The amplitude spectrum is calculated from the data in Fig. 3 with LSM. The weak alias peaks in $m = 0$ panel originate from sensor mismatch and aliasing effect due to the outer rotation. The latter acts like a sampling frequency and therefore projects the AMRI wave to $m = 0$.

the noise energies over multiple domain variables. For the present example this means that the distortions are projected into higher frequencies f , higher m 's and larger k 's. Since the signal of interest remains in the same spectral corridor, its signal amplitude becomes more clear, because of the "reduced" local noise.

4.3 Analyzing 2D sunspot data

Since the beginning of the 17th century systematic visual observations of sun spots are available which allow to investigate dynamic processes taking place in the sun. The appearance of sunspots on the surface of the Sun depends on the level of solar activity and therefore it renders some fundamental features of the underlying solar dynamo, such as the 11 yrs solar cycle. Since the beginning of the 1820's observational data is available in terms of a two dimensional time series that exhibits a periodic wing-like pattern essentially symmetric with respect to the Sun's equator. The sunspot butterfly diagram emerges and summarizes the individual sunspot groups appearing at a certain time and latitude on the Sun for the past 190 years. Additionally, Figure 5 depicts the assigned field polarity order indicated by color (gray or black). The segmentation procedure followed the suggestions from Leussu et al. (2016), but with some simplifications leading only to minor miss-assignments for individual sunspot groups. The field polarity $P(Y, L) \in \{-1, 1\}$ gives the arrangement of leading North/South polarity of a sunspot group, depending on the year Y and the mean latitude L . This polarity is changing approximately each 11 years which is related to Schwabe's cycle. The full period of 22 yrs is then called the Hale cycle.

The data is taken "as-is" from Leussu et al. (2017), which originates from several sources with different qualities, i. e. the Royal Greenwich Observatory – USAF/NOAA(SOON)¹(Clette et al. 2014; Willis et al. 2016), Schwabe²(Arlt et al. 2013) and Spoerer³(Diercke et al. 2015) data sets. A detailed discussion of the data collection is given by Leussu et al. (2016, 2017) and the referenced literature.

¹Available at

<http://solarscience.msfc.nasa.gov/greenwch.shtm1>

²Available at

<http://www.aip.de/Members/rarlt/sunspots/schwabe>

³the reader might also refer to the historic publications Spoerer (1889); Spoerer & Maunder (1890)

The following example deduces the spectral decomposition from this unevenly sampled binary data set $P(Y, L)$ to identify typical periods and their modulation. In contrast to the two examples above, the sunspot data set consists of real arbitrary sampling in both, time and space, giving the most general scenario for the LSM.

The starting point for the subsequent analysis is the simplified segmentation of the butterfly diagram reassigning the field polarity. The segmentation takes place by optimizing the distance d of each point $P(L, Y)$ with respect to the segmentation line

$$L(Y) = \begin{cases} m_1 (Y - T_0) & m_1 < 0, L > 0 \\ m_2 (Y - T_0) & m_2 > 0, L \leq 0 \end{cases},$$

which is a piece wise linear function with the intersection point $\{T_0, 0\}$. The dependent variables Y and L describe the time in years and latitude in degrees respectively. The individual slopes $m_1, m_2 < 12$ deg/yr are assigned on the northern and southern hemispheres, respectively. The initial value of the temporal shift $T_{0g} \approx 1835 + 11g$ considers the group id g to move forward in the data set. The optimization then minimizes the penalty function $p \sim e^{-d(1+m/5)}$ as a measure of inverse distance between points and corresponding segmentation lines and minimal slope. Figure 6 depicts the optimization group of the last 30 yrs, where the gray line indicates the initial condition and red line the optimized result. The subdivision is straight forward but not perfect, indicated for example by several points around the year 1990 at $\pm 50^\circ$ latitude which might be assigned differently when doing the suggested segmentation by Leussu et al. (2017, Fig. 2). However, with a total sum of $\mathcal{O}(2.8 \cdot 10^5)$ observed sunspots, it is unlikely that such single distortions change the character of the spectrum. The final segmentation is depicted in Figure 5 where 18 individual cycles subdivided by a ">" - shaped separation area are shown.

By observing the slopes of segmentation lines and the individual shapes of the patches a slight asymmetry between northern and southern hemisphere can be recognized. This becomes clear in the different average values of the slopes (see Table 1). Figure 5 also indicates a modulation of the maximum latitude of individual cycles with a period of ~ 200 years which may be related to the Suess de Vries cycle.

The spectral LSM decomposition is based on the defi-

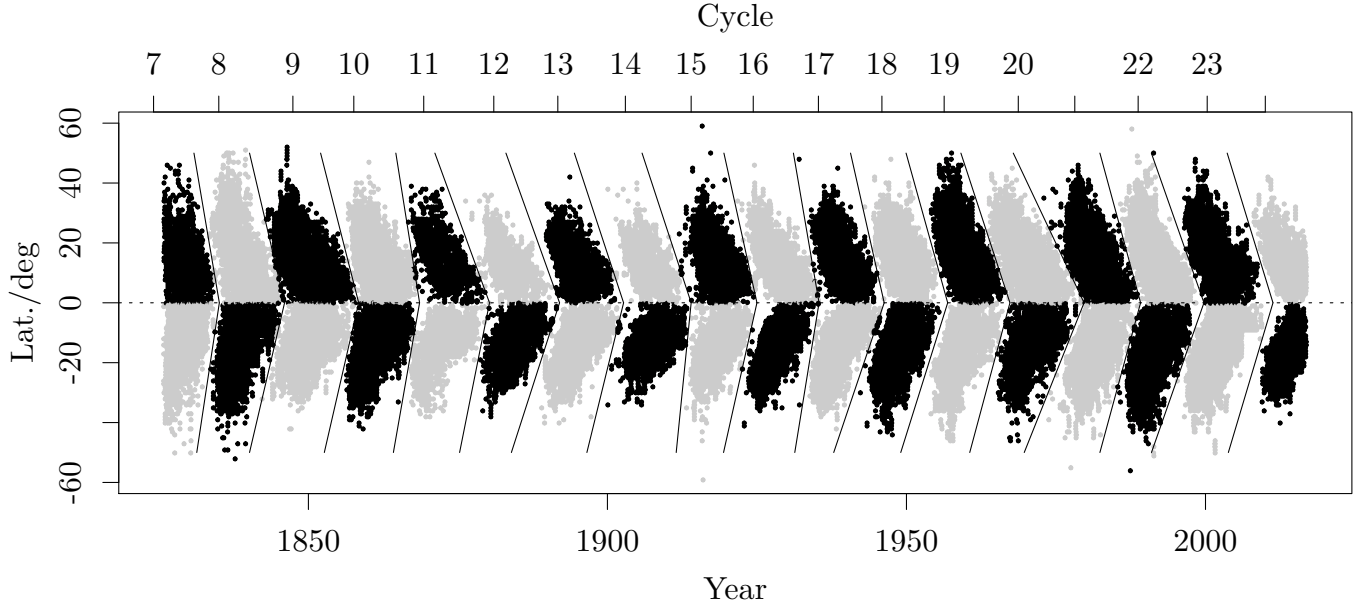


Figure 5: Butterfly diagram of the sunspot data. The separation of the individual wings took place according to the proposed procedure presented in Leussu et al. (2016). The colored patches indicate the changing polarity of each cycle. The tilted segmentation lines depict the optimized borders between two cycles.

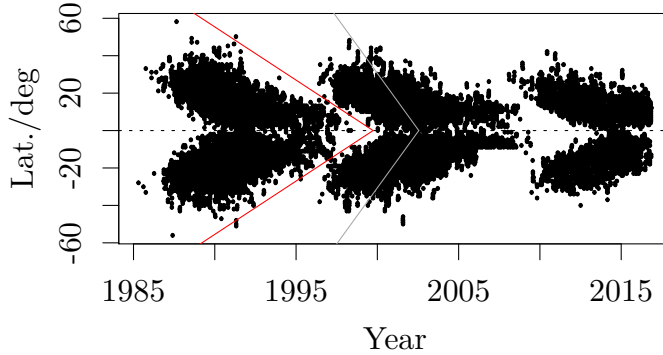


Figure 6: Optimization of segmentation lines. Black dots represent the sunspot positions over time. The gray line indicate the initial condition for the fit whereas the red one depicts the result of the optimization.

Table 1: Parameters of Segmentation Lines. The slopes $m_{1,2}$ are given in deg/year

T_0/Year	m_1	m_2	T_0/Year	m_1	m_2
1835.1	-11.8	13.2	1946.3	-8.9	5.9
1846.0	-8.5	8.5	1956.9	-7.2	6.4
1858.4	-7.9	8.7	1967.3	-6.1	7.4
1868.6	-12.6	11.4	1979.7	-4.2	5.0
1880.3	-5.5	10.0	1989.1	-7.3	7.3
1892.0	-5.6	6.2	1999.7	-5.7	5.7
1902.7	-6.1	8.1	2011.3	-6.5	6.7
1914.0	-6.1	20.0			
1925.0	-9.1	9.0			
1935.4	-11.7	12.3			
Average $\bar{m}_{1,2}$				-7.68	8.94

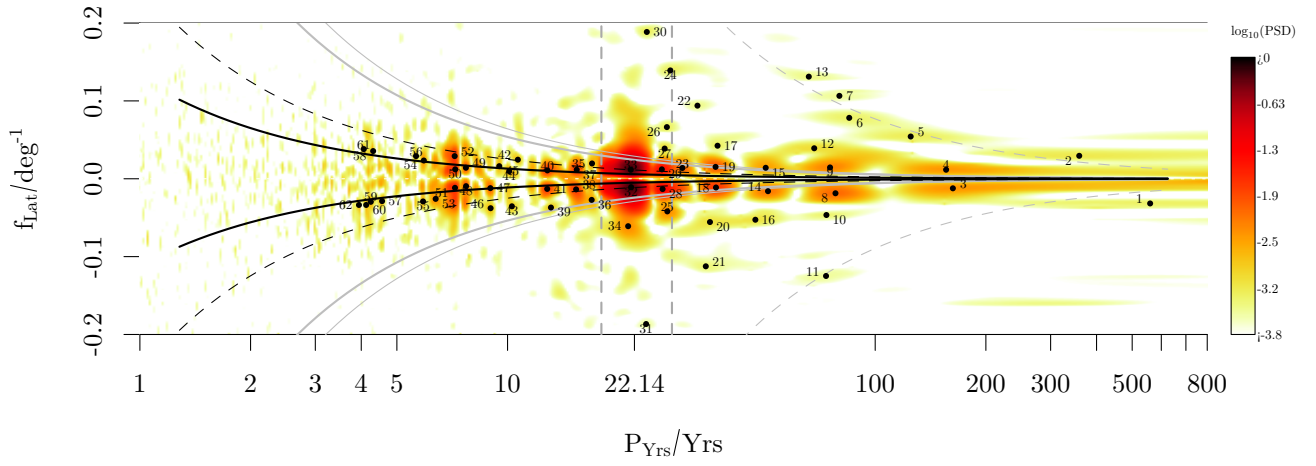


Figure 7: 2D LSM spectrum of the sunspot data. The numbering of the individual maxima correspond to the ID in Table 3. The curved lines follow a path of constant phase velocity with $v = (f_{\text{Lat}} P_{\text{Yrs}})^{-1} = \text{const.}$ indicating a wave structure with a certain time dependence. The bold black lines depicts the mean waves with $v = \bar{m}_{1,2}$, whereas the dashed lines follow a perfect sinusoidal wave defined by the dominant points $ID \in \{32, 33\}$. The range of the solar cycle period is given by the vertical dashed grey lines.

nition of a two dimensional wave model

$$P(Y, L) \sim A \cdot \cos(\omega_{\text{Yrs}} Y + \omega_{\text{Lat}} L + \tau^*) + \quad (44)$$

$$B \cdot \sin(\omega_{\text{Yrs}} Y + \omega_{\text{Lat}} L + \tau^*) + \epsilon,$$

where P is given by the assigned patch polarity. To show the advantage and robustness of LSM the raw data is supplied without any further preprocessing. The selected frequencies $\omega_{\text{Yrs},n}, \omega_{\text{Lat},n} \propto n^{-1}$ are given on a rectangular grid with inverse distance so that the periods ω^{-1} are distributed uniformly alongside the consecutive counter n . Furthermore, the frequency resolution in the range of $|\omega_{\text{Lat}}| = 0$ is selected finer to better resolve this region.

Figure 7 gives the resulting spectral decomposition in a reciprocal log-scale plot to focus on the periods. Each of the selected peaks (numbered black dots) provides a FAP value of $p < 10^{-10}$, meaning that these periods are significantly different from noise level. Each of these points originate from a maximization of the local amplitude value as a subsequent refinement. The numbering corresponds to the peak identifier ID in Table 3. The binary order information $\{-1, 1\}$ introduces higher harmonics into the spectrum, which do also appear with a significantly low FAP value. Table 3 summarizes peaks with $P_{\text{Yrs}} > 3$ yrs and a certain strength. A detailed discussion about the definition of the noise level in case of binary input data and the proper peak selection is left for future work.

The interpretation of the spectrum can be given in two ways. First, a purely temporal frequency analysis provides good agreement between the peaks found and the common known periods. Table 2 summarizes the major outcome in comparison with literature. For example the 22 yrs Hale cycle varies from 18... 28 yrs (Usoskin (2017)) which is identified by the two main peaks $ID \in \{32, 33\}$. Since the solar cycle is modulated, refer to Hathaway (2015), it is natural that a broad spectrum with many harmonics becomes present. These subsequent patterns are related to a set of local maxima mainly collapsing on a horizontal line at $|f_{\text{Lat}}| \approx 1.4 \cdot 10^{-2} \text{ deg}^{-1}$. The interpretation is, that the complex structure of the individual wing-shapes of the butterfly diagram with different widths, heights and orientation, correspond to a main period $P_{\text{Hale}} = 21.634$ yrs and some harmonics. Next to that we can identify typical periods which are related to the Gleissberg process (see Table 2). The short periods in the range of $P \approx 7.2$ yrs are consistent with the data

provided by Prestes et al. (2006), Kane (1997) and partly with Deng et al. (2020).

Second, the latitudinal dimension of the spectrum spreads the peaks vertically. This is a great advantage compared to a purely 1D analysis, where all signal would be projected on the $f_{\text{Lat}} = 0$ line. In this case individual peaks, i. e. $ID \in \{17, 21, 25, 34, 27, \dots\}$ would collapse on the ordinate in a single domain analysis. Furthermore, Figure 5 can be interpreted as a set of modulated waves propagating towards the equator. The two dimensional LSM decomposes the frequencies and gives access to the properties of such waves.

If a single large peak corresponding e. g. to $P \approx 22$ yrs and with $|f_{\text{Lat}}| > 0$ would be related to a perfect sinusoidal wave, the associated complex texture of moving patterns is neglected. In contrast to that, a constant pattern, i. e. a fixed group of sunspots drifting towards the equator, would find its representation in a variety of peaks along a line of constant phase velocity, $v = (f_{\text{Lat}} P_{\text{Yrs}})^{-1} = \text{const.}$. If such a pattern slowly changes over time, which is clearly the case in Figure 5, the corresponding v -line becomes the center frequency of an amplitude modulated wave. Hereby, the average phase velocity, represented by the v -line, keeps the same but is accompanied by side bands to the left and to the right. This can be seen as an n D amplitude modulation, where the v -line is the carrier frequency.

Figure 7 provides some of the v -lines related to typical referenced processes. Starting with the Hale-cycle, which is identified by $P_{\text{Hale}} = 21.634$ yrs and $f_{\text{Lat}} = 1.152 \cdot 10^{-2} \text{ deg}^{-1}$ ($ID \in \{32, 33\}$), we obtain the typical phase velocity of $v_{\text{Hale}} = 4.012 \text{ deg/yr}$. This single phase approximation assumes a perfect sinusoidal wave represented by a single peak. Nevertheless, the dashed black line indicates the corresponding v -line which includes the main peak of the diagram but passes many others. On the other hand, the average slopes of the segmentation lines for the northern and southern hemisphere can be deduced from Figure 5. Here the mean values, compared with Table 1 result in the mean slope velocities $\bar{v}_{1,2} = \bar{m}_{1,2}$ which correspond to the black solid lines. As the butterfly diagram indicates a time varying pattern (of the individual wings) it is quite natural, that the mean phase velocity is surrounded by side bands. The concept of side band modulation assigns such peaks to the same a complex wave pattern, like the Hale-wave.

Table 2: Common Peaks. Period values are given in years. Values above 100 yrs are affected by the low period resolution caused by the limited time span of sunspot data. The results from Prestes et al. (2006) refer to Schwabe cycle and therefore are doubled.

Process	Common Period	From spectrum	Ref.
Eddy	515	559	1
	350	359	1
Hale (Schwabe)	22.14 (11.07)	21.63 ± 2.5	2
	18...28 (2)		
Gleissberg	88 (80...150)	78, 85, 125, 156	1,2
–	126	125	3
–	2×3.6	7.2	4
–	2×3.9	7.7	4,5

(1) McCracken et al. (2013); (2) Usoskin (2017); (3) Ogurtsov et al. (2002); (4) Prestes et al. (2006, Fig. 6); (5) Kolotkov et al. (2015).

Hereby the (carrier) v -lines touch certain local maxima, i. e. at $P \approx 4$ or $ID \in \{57 \dots 62\}$, so they can be assumed to map the most realistic wave structure for the butterfly diagram in contrast to a purely sinusoidal Hale - wave pointed out above. The argument about the mapping of certain points to a characteristic v -line is supported by the fact that in this case \bar{v} originates from the space-time analysis of Figure 5. The conclusion is that the Hale-cycle, finding its main period at P_{Hale} might be described as a modulated set of waves with minor prominent harmonics. If so, peaks arranged around the characteristic v -line such as $ID \in \{51 \dots 54\}$ or $ID \in \{48, 49\}$, are directly coupled with the Sun cycle. These individual side bands $ID \in \{51 \dots 54\}$ are covered by the results of Prestes et al. (2006) investigating geomagnetic indices and sunspot number time series. The peaks $ID \in \{48, 49\}$, are supported by findings from Kolotkov et al. (2015) analyzing 10.7 cm radio flux measurements, helioseismic frequency shift and the sunspot area. Short term oscillations ($ID \in \{17, 22, 23, 53\}$ as doubled period) are obtained by Deng et al. (2020) from grouped solar flare as well as sun spot number time series.

Despite the modulated structure of the wings, it might be of interest to focus on their mean path from which a time dependent drift velocity can be deduced. From the standard law for this equatorial drift, see Hathaway (2011, Eq. (4)), the mean velocity $\bar{v} = 1.8622 \text{ deg/yr}$ follows from the average (centroid) position, $\bar{\lambda}(t) = 28^\circ e^{-12t/90}$ of the sunspots as function of time t in a $T = 12 \text{ yrs}$

range. The corresponding bold gray v -line in Figure 7 assigns several numbered and unnumbered peaks to the motion of sunspots. The neighboring thin solid gray line is defined by $\bar{v} = 1.56 \text{ deg/yr}$ as suggested by Li et al. (2001) investigating the same process of equatorial drift.

As a speculation about other present waves, the dashed gray line defined by the peaks $ID = \{2, 5, 6, 7, 13\}$ might be related to a Gleissberg process. The corresponding line in the lower half plane of Figure 7 is not symmetric indicating the asymmetry between the hemispheres. And finally a remaining v -line could be defined by the points $ID = \{4, 12, 17, 22, 24, 30\}$ and $ID = \{3, 10, 16, 20, 21, 31\}$ which might belong to another (unidentified) process.

Taking only the raw data of the sunspots (time and latitude) into account, LSM allows the analysis of complex dependencies between individual spectral peaks due to the idea of a modulated traveling wave. The result of LSM was verified with characteristic peaks obtained from a variety of references based on complementary data sets. Since the features of the sunspots are related to the solar dynamo the analysis has the potential to obtain a better insight into the magnetic field generating processes in the tachocline with respect to the differential rotation.

5 Conclusions

In the present work a multidimensional extension of the Lomb-Scargle method is developed. The key aspect is the

redefinition of phase argument to $\vec{\phi}_{\text{new}} = \vec{\omega} \cdot \vec{t} - \tau^*$. We suggest using a modified shifting parameter τ^* in contrast to the traditional approach which shifts the ordinate $\phi_{\text{orig}} = \omega \cdot (t - \tau)$ instead of the phase. This enables multivariate modeling with one single scalar value τ^* for all independent variables as there is always a shifting parameter τ^* for which $\int_a^b \sin(\phi(t)) \cos(\phi(t)) dt$ vanishes on any interval $[a, b]$.

The examples from Section 4 underline the strengths of the developed procedure in a consecutive way. First the application on ideal two dimensional test data shows the ability to analyze fragmented time series. Here the sampling remains regular meaning $t = nT_0$ with $n \in \mathbb{N}$, but with $n_i - n_{i+1} \neq 1$ as an incomplete set of locations to describe missing values. A second quasi similar situation is given in the experimental data set of UDV measurements, expect a certain jitter. The dimensionality in this example was extended to \mathbb{R}^3 to decompose the wave parameters in frequency f , symmetry m and spatial frequency k .

As the third analysis, the sunspot data sets represent the most general case of non-evenly sampling. Taking only the time series of positions into account, LSM is able calculate the spectrum on a individual frequency grid pronouncing the low frequencies close to zero. The assignment of $\{-1, 1\}$ to each data point is a minor modification so the data can be assumed as binary raw data. The spectral decomposition with LSM shows the characteristic footprint of waves and its dynamics present in the butterfly diagram. The time frequency spectrum itself provides the commonly known frequencies, i.e. Hale-Cycle or Gleissberg process. The second frequency f_{Lat} provides information about the minor peaks which are spread out into the latitudinal domain. Moreover, from these values the sunspot drift motion can be calculated using a characteristic v -line with its side bands. For validation of these new procedure different measures are compared with characteristic peaks in the spectrum: (i) the mean slopes of the segmentation lines from Figure 5 can be interpreted as average phase velocity. The corresponding v -line nicely assigns several peaks to the dominant Hale cycle. (ii) the individual values for latitude migration from Li et al. (2001); Hathaway (2011) do form a v -line describing sunspot motion. In any instance the spectral signature of a moving complex pattern becomes evident by a center line of constant phase velocity and its side

bands, containing the temporal dynamics (modulation) of the motion.

With respect to the evaluation of measurement results, the noise rejection $\epsilon_{\text{LS}} \propto 4N^{-0.5}/\pi$ and confidence intervals (Δa_k and Δb_k) of model parameters a_k and b_k are delineated. To emphasize the advantages of the LSM the traditional Fourier mode decomposition is compared. It turned out that the systematic error ϵ_{T} does not vanish for FT based methods with increasing number of samples on a fixed interval T , which finally lead to the common leakage effect as seen in Figure 2c. Here the signal amplitudes are distributed on an area of neighboring pixels. We conclude that the standard orthogonal mode related procedures do not represent a consistent estimator for model parameters a_k and b_k . Whereas the introduction of τ^* in LSM leads to a consistent estimator with $\epsilon_{\text{T}} = 0$ even for higher dimensions. Finally, it was shown that LSM converges to the true model parameters with increasing number of samples and provides a better noise rejection ($\epsilon_{\text{LS}} < \epsilon_{\text{FS}}$) as well.

Acknowledgements

The authors like to thank Rainer Arlt from Astrophysical Institute Potsdam providing the sunspot data and Andre Gieseke from HZDR for many fruitful discussions. F. Garcia kindly acknowledges the Alexander von Humboldt Foundation for its financial support.

References

- Al-Ani, M. & Tarczynski, A. 2012, Signal Processing, 92, 2484
- Arlt, R., Leussu, R., Giese, N., Mursula, K., & Usoskin, I. G. 2013, Monthly Notices of the Royal Astronomical Society, 433, 3165
- Babu, P. & Stoica, P. 2010, Digital Signal Processing, 20, 359
- Baluev, R. V. 2008, Monthly Notices of the Royal Astronomical Society, 385, 1279
- Baluev, R. V. 2013a, Monthly Notices of the Royal Astronomical Society, 436, 807

- Baluev, R. V. 2013b, *Astronomy and Computing*, 3-4, 50
- Barning, F. J. M. 1963, *Bulletin of the Astronomical Institutes of the Netherlands*, 17, 22
- Cadena, C., Carlone, L., Carrillo, H., et al. 2016, *IEEE Transactions on Robotics*, 32, 1309
- Clette, F., Svalgaard, L., Vaquero, J. M., & Cliver, E. W. 2014, *Space Science Reviews*, 186, 35
- Cohen, L. 1995, *Time-Frequency Analysis*, Prentice Hall signal processing series (Englewood Cliffs, N.J: Prentice Hall PTR)
- Cumming, A., Marcy, G. W., & Butler, R. P. 1999, *The Astrophysical Journal*, 526, 890
- Deng, H., Mei, Y., & Wang, F. 2020, *Research in Astronomy and Astrophysics*, 20, 022
- Diercke, A., Arlt, R., & Denker, C. 2015, *Astronomische Nachrichten*, 336, 53
- Eyer, L. & Bartholdi, P. 1999, *Astronomy and Astrophysics Supplement Series*, 135, 1
- Fessler, J. & Sutton, B. 2003, *IEEE Transactions on Signal Processing*, 51, 560
- Fessler, J. A. 2002, 11
- Frydman, L., Lupulescu, A., & Scherf, T. 2003, *Journal of the American Chemical Society*, 125, 9204, publisher: American Chemical Society
- Geneva, P., Eckenhoff, K., & Huang, G. 2018, in 2018 IEEE International Conference on Robotics and Automation (ICRA) (Brisbane, QLD: IEEE), 1–6
- Giraudeau, P. & Frydman, L. 2014, *Annual Review of Analytical Chemistry*, 7, 129
- Gonzalez, R. C. & Woods, R. E. 2008, *Digital Image Processing*, 3rd edn. (Prentice Hall)
- Greengard, L. & Lee, J.-Y. 2004, *SIAM Review*, 46, 443
- Haacke, E. 1999, *Magnetic Resonance Imaging: Physical Principles And Sequence Design* (John Wiley and Sons)
- Hathaway, D. H. 2011, *Solar Physics*, 273, 221
- Hathaway, D. H. 2015, *Living Reviews in Solar Physics*, 12, 4
- Hocke, K. 1998, *Annales Geophysicae*, 16, 356
- Horne, J. H. & Baliunas, S. L. 1986, *The Astrophysical Journal*, 302, 757
- James, J. 2011, *A Student's Guide to Fourier Transforms: with Applications in Physics And Engineering*, 3rd edn. (Cambridge University Press)
- Jerri, A. J. 1977, *Proceedings of the IEEE*, 65, 1565
- Kane, R. P. 1997, *Annales Geophysicae*, 15, 1581
- Kolotkov, D. Y., Broomhall, A.-M., & Nakariakov, V. M. 2015, *Monthly Notices of the Royal Astronomical Society*, 451, 4360
- Kovács, G. 1981, *Astrophysics and Space Science*, 78, 175
- Leroy, B. 2012, *Astronomy & Astrophysics*, 545, A50
- Leussu, R., Usoskin, I. G., Arlt, R., & Mursula, K. 2016, *Astronomy & Astrophysics*, 592, A160
- Leussu, R., Usoskin, I. G., Pavai, V. S., et al. 2017, *Astronomy & Astrophysics*, 599, A131, publisher: EDP Sciences
- Li, K. J., Yun, H. S., & Gu, X. M. 2001, *The Astronomical Journal*, 122, 2115, publisher: IOP Publishing
- Liu, Q. & Nguyen, N. 1998, *IEEE Microwave and Guided Wave Letters*, 8, 18
- Lomb, N. R. 1976, *Astrophysics and Space Science*, 39, 447
- Mathias, A., Grond, F., Guardans, R., et al. 2004, *Journal of Statistical Software*, 11, 1
- McCracken, K., Beer, J., Steinhilber, F., & Abreu, J. 2013, *Space Science Reviews*, 176, 59
- Mortier, A., Faria, J. P., Correia, C. M., Santerne, A., & Santos, N. C. 2015, *Astronomy & Astrophysics*, 573, A101
- Munteanu, C., Negrea, C., Echim, M., & Mursula, K. 2016, *Annales Geophysicae*, 34, 437, publisher: Copernicus GmbH

- Ogurtsov, M. G., Nagovitsyn, Y. A., Kocharov, G. E., & Jungner, H. 2002, 24
- Oppenheim. 1999, *Discrete-Time Signal Processing*, 2nd edn. (Prentice Hall)
- Parzen, E. 1962, *Stochastic Processes*, ed. E. L. Lehmann, *Holden Day Series in Probability and Statistics* (San Francisco: Holden-Day)
- Press, W. H. & Rybicki, G. B. 1989, *The Astrophysical Journal*, 338, 277
- Prestes, A., Rigozo, N. R., Echer, E., & Vieira, L. E. A. 2006, *Journal of Atmospheric and Solar-Terrestrial Physics*, 68, 182
- Scargle, J. D. 1982, *The Astrophysical Journal*, 263, 835
- Seilmayer, M. 2019, *Common Methods of Spectral Data Analysis*
- Seilmayer, M., Galindo, V., Gerbeth, G., et al. 2014, *Physical Review Letters*, 113, 024505
- Seilmayer, M., Gundrum, T., & Stefani, F. 2016, *Flow measurement and instrumentation*, 48, 74
- Shannon, C. E. 1949, *Proceedings of the IRE*, 37, 10
- Spoerer, F. W. G. & Maunder, E. W. 1890, *Monthly Notices of the Royal Astronomical Society*, 50, 251
- Spoerer, G. 1889, *Bulletin Astronomique, Serie I*, 6, 60
- Sudars, K. 2010, *Automatic Control and Computer Sciences*, 44, 199
- Thompson, J. K. & Tree, D. R. 1980, *Journal of Sound and Vibration*, 71, 531
- Townsend, R. H. D. 2010, *The Astrophysical Journal Supplement Series*, 191, 247
- Usoskin, I. G. 2017, *Living Reviews in Solar Physics*, 14, 3
- VanderPlas, J. T. 2017, *The Astrophysical Journal*, 236
- Weisstein, E. W. 2019, *Orthogonal Functions*
- Willis, D. M., Wild, M. N., & Warburton, J. S. 2016, *Solar Physics*, 291, 2519
- Zechmeister, M. & Kürster, M. 2009, *Astronomy & Astrophysics*, 496, 577

Appendix

A OMD as a non-consistent estimator

In the following, only signals $s(t) \in \mathbb{R}$ described in terms of a finite set of individual frequency components $\omega_k, 0 \leq k \leq M$ ($k \in \mathbb{N}^+$), are considered. Furthermore, band limitation is assumed so that there exists an upper maximum frequency $\omega_k < \omega_{\max}$.

The analysis is based on the trigonometric model definition from equation (2) with the coefficients $a_k, b_k \in \mathbb{R}$. The model misfit $\epsilon(t)$ is defined by the difference between the observed signal $s(t)$ and the assumed model function (2) as seen in equation (3). It follows Eq. (4)

$$s(t) = \sum_{k=0}^M (a_k \cos(\omega_k t) + b_k \sin(\omega_k t) + \epsilon_k(t)),$$

the signal as sum of a trigonometric model with M coefficients and individual error values. The total model misfit $\epsilon(t) = \sum_k \epsilon_k(t)$ originates from measurement uncertainties with unknown distribution.

However, the sine and cosine functions are assumed as an orthonormal basis, which is valid for the infinite integral, as seen in Section 2.2. To shorten the explanations the derivation refers only to the cosine term and neglects the corresponding sine term, which can be always achieved in similar manner.

To show the effects of OMD applied to discrete sampled functions, e. g. taking time series from measurements, the next passage derives the sampling series and its discrete model representation.

In general, a continuous signal can be described as a function defined for every $-\infty < t < \infty$. But a realistic measurement or observation $y(t)$ of such a process takes place in the range from $t = 0$ to arbitrary time $t = T$. Therefore, we associate to the measurement a windowed

signal $s_w(t)$ defined for every $-\infty < t < \infty$ as

$$s_w(t) = (y(t) + \epsilon(t)) \cdot w(t)$$

$$\text{with } w(t) = \begin{cases} 1 & 0 \leq t < T \\ 0 & \text{otherwise} \end{cases} \quad (\text{A.1})$$

where the sampling error $\epsilon(t)$ is included. The window function $w(t)$ ensures the finite observation time $0 \leq t < T$ but leave the infinite definition range untouched.

The sampling procedure, described in the next step, relies on the Dirac distribution and its properties. The Dirac impulse is defined as

$$\delta(t) = \begin{cases} \infty & t = 0 \\ 0 & t \neq 0 \end{cases} \text{ with } \int_{-\infty}^{\infty} \delta(t) dt = 1. \quad (\text{A.2})$$

The so-called sifting property

$$\int_{-\infty}^{\infty} \delta(t - \tau) \cdot \phi(t) dt = \phi(\tau), \quad (\text{A.3})$$

can be expressed for every function $\phi(t)$. Using this identity the convolution function

$$\Psi(t) = \sum_{n=-\infty}^{\infty} \delta(t - nT_s) \quad (\text{A.4})$$

helps to describe the sampling of the signal $s_w(t)$ with sampling rate T_s .

The continuous description of the sampling series

$$A(t) = s_w(t)\Psi(t) \quad (\text{A.5})$$

mathematically models the sampling which takes place while taking a time series measurement of a physical process.

According to the theory of orthogonal function decomposition – briefly described and proven by Cohen (1995, Chap. 15) – the individual model coefficients of Eq. (2)

$$a_k = \frac{2}{T} \int_{-\infty}^{\infty} y(t) \cos(\omega_k t) dt \quad (\text{A.6})$$

$$\text{and } b_k = \frac{2}{T} \int_{-\infty}^{\infty} y(t) \sin(\omega_k t) dt \quad (\text{A.7})$$

can be recovered by integrating over the model function.

In order to estimate the coefficients a_k, b_k of the model equation (2) the integration of (A.6) and (A.7) has to be carried out on the sampled series $A(t)$ representing the acquired data. Assuming that the trigonometric model $y(t)$ approximates the sampling series $A(t)$ in the limit $\epsilon(t) \rightarrow 0$:

$$a_k = \frac{2}{T} \int_{-\infty}^{\infty} y(t) \cos(\omega_k t) dt$$

$$\approx \frac{2}{T} \int_{-\infty}^{\infty} A(t) \cos(\omega_k t) dt$$

$$= \frac{2}{T} \int_{-\infty}^{\infty} (y(t) + \epsilon(t)) w(t) \sum_{n=-\infty}^{\infty} \delta(t - nT_s) \cos(\omega_k t) dt, \quad (\text{A.8})$$

and by factorizing and exchanging the sum with the integral

$$a_k = \frac{2}{T} \sum_{n=-\infty}^{\infty} \int_{-\infty}^{\infty} \underbrace{(y(t) + \epsilon(t)) w(t) \cos(\omega_k t) \delta(t - nT_s)}_{\text{sifting property (A.3)}} dt$$

$$= \frac{2}{T} \sum_{n=-\infty}^{\infty} (y(nT_s) + \epsilon(nT_s)) w(nT_s) \cos(\omega_k nT_s), \quad (\text{A.9})$$

where the applied sifting property of the Dirac distribution achieves the sampling at discrete time instances nT_s . Due the definition of the rectangular window function $w(t)$ the sum with $nT_s < 0$ and $nT_s > T$ is exactly zero, which lead to a finite summation range. With the identity of the total number of samples taken, $N = T/T_s$, the coefficient a_k reads as follows

$$a_k = \frac{2}{T} \sum_{n=0}^{N-1} (y(nT_s) + \epsilon(nT_s)) \cos(\omega_k nT_s)$$

$$= \frac{2}{T} \sum_{n=0}^{N-1} \left(\sum_{j=0}^M (a_j \cos(\omega_j nT_s) + b_j \sin(\omega_j nT_s) + \epsilon(nT_s)) \right) \cos(\omega_k nT_s) \quad (\text{A.10})$$

Figure 1 sketches the scenario with $T_s = f_s^{-1}$ as the sampling period and $T > 2\pi/\omega_0$. With respect to the integrals (A.6) and (A.7) the dashed right area causes

errors in two ways, when QDT is carried out. First, the energy of that amplitude is spread into the next neighboring integer ks and second the truncation error (dashed area) causes a mismatch of a_k (and b_k) which only depends on T but *not* on the amount of sampling points N used.

In the following steps, the coefficients $k \neq j$ are neglected, since they are projected in the error $\epsilon(t)$. The remaining k -th set of parameters $k = j$ is sufficient to derive the concluding points (i)-(iv) from Section 2.2.

A.1 Properties of the truncation error – (i), (ii)

Considering the Fourier decomposition of the sampling series $A(t)$

$$\begin{aligned} & \int_0^T \sum_{n=0}^{N-1} s_w(nT_s) \delta(t - nT_s) \cos(\omega_k nT_s) dt \\ &= \int_0^T \delta(t - nT_s) dt \sum_{n=0}^{N-1} a_k \cos^2(\omega_k nT_s) \\ &+ b_k \sin(\omega_k nT_s) \cos(\omega_k nT_s) + \epsilon_k \cos(\omega_k nT_s), \quad (\text{A.11}) \end{aligned}$$

which can be rewritten with respect to the window function $w(t)$. The latter enables the limitation of the integration and summation boundaries. Next, by applying the sifting property (A.3) the continuous time series becomes independent from time so that

$$\begin{aligned} \sum_{n=0}^{N-1} s_w(nT_s) \cos(\omega_k nT_s) &= \sum_{n=0}^{N-1} [a_k \cos^2(\omega_k nT_s) \\ &+ b_k \sin(\omega_k nT_s) \cos(\omega_k nT_s) \\ &+ \epsilon_k \cos(\omega_k nT_s)] \end{aligned} \quad (\text{A.12})$$

describes the measured (sampled) data points at time instances nT_s of the signal. The expression above represents the well known sum of the k -th cosine term of discrete Fourier series. The corresponding sine term is defined in similar manner.

With respect to the trigonometric identities $\cos^2(x) = \frac{1}{2}(1 + \cos(2x))$ and with $\sin(x) \cos(x) = \frac{1}{2} \sin(2x)$ Equation (A.12) becomes

$$\sum_{n=0}^{N-1} s_w(nT_s) \cos(\omega_k nT_s) = \sum_{n=0}^{N-1} \left(\frac{a_k}{2} (1 + \cos(2\omega_k nT_s)) + \frac{b_k}{2} \sin(2\omega_k nT_s) + \epsilon_k \cos(\omega_k nT_s) \right) \quad (\text{A.13})$$

$$\frac{2}{N} \sum_{n=0}^{N-1} s_w(nT_s) \cos(\omega_k nT_s) = a_k \left(1 + \frac{1}{N} \sum_{n=0}^{N-1} \left[\cos(2\omega_k nT_s) + \frac{b_k}{a_k} \sin(2\omega_k nT_s) \right] \right) + \frac{2}{N} \sum_{n=0}^{N-1} \epsilon_k \cos(\omega_k nT_s) \quad (\text{A.14})$$

Assuming $b_k \approx 0$, which corresponds to a pure $\cos(x)$ signal the error can be divided into two components

$$\begin{aligned} \epsilon_T &= \frac{1}{N} \sum_{n=0}^{N-1} \cos(2\omega_k nT_s) \\ &= \frac{1}{N} \left(\underbrace{\sum_{n=0}^{N_{2\pi}} \cos(2\omega_k nT_s)}_{=0} + \sum_{n=N_{2\pi}+1}^{N-1} \cos(2\omega_k nT_s) \right), \end{aligned} \quad (\text{A.15})$$

from which the first vanishes because it covers an integer number of periods ω_k . The right one consequently describes the truncation error with respect to a $2\omega_k$ frequency as given in the gray area in Figure 1. A Taylor

series decomposition gives

$$\begin{aligned} \epsilon_T &= \frac{T_s}{T} \sum_{n=N_{2\pi}+1}^{N-1} \left(1 - \frac{1}{2!} (2\omega_k n T_s)^2 + \underbrace{\frac{1}{4!} (2\omega_k n T_s)^4 - \dots}_{\rightarrow 0} \right) \quad \text{The last term} \\ &\approx \frac{T_s}{T} \left(\Delta N - 2 (\omega_k T_s)^2 \sum_{n=N_{2\pi}}^{N-1} n^2 \right) \end{aligned} \quad (\text{A.16})$$

which is reduced further with $\sum_{n=1}^N n^2 = \frac{N(N+1)(2N+1)}{6}$ and $T_s = T/N$

$$\begin{aligned} \epsilon_T &\approx \frac{\Delta N}{N} - 2 (\omega_k T)^2 \frac{\Delta N (\Delta N + 1) (2\Delta N + 1)}{6N^3} \\ &\approx \frac{\Delta N}{N} \left(1 - 2 (\omega_k T)^2 \left(\frac{2\Delta N^2}{6N^2} + \underbrace{\frac{3}{6N^2} + \frac{1}{6N^2 \Delta N}}_{\rightarrow 0} \right) \right) \\ &\approx \frac{\Delta N}{N} \left(1 - \frac{2}{3} (\omega_k T)^2 \left(\frac{\Delta N}{N} \right)^2 \right) \quad \text{with } N = T/T_s \\ &\approx \frac{\Delta \varphi}{T} \leq 0.2 \end{aligned} \quad (\text{A.17})$$

so that ϵ_T becomes independent of the sampling rate T_s . The ‘‘time phase’’ $\Delta \varphi$ covers the range marked as gray area in Figure 1. The maximum value of $\epsilon_T \leq 0.2$ originates from the $\cos(2\omega_k n T_s)$ -term if only one period plus truncation fits into the integration window. Moreover equation (A.17) implies, that a higher sampling frequency – which gathers more information from the process – will not lead to a more precise approximation of a_k (and of course b_k). Therefore, the QDT (or even the Fourier series decomposition) is *not* a consistent estimator for amplitude and phase, because it will not converge

$$\lim_{N \rightarrow \infty} \sum_{n=0}^{N-1} y(n T_s) \cos(\omega_k n T_s) \neq a_k \quad (\text{A.18})$$

towards the ‘‘true’’ a_k for a given finite T . Instead of that it converges in the limit of $T \rightarrow \infty$.

A.2 Confidence intervals of model parameters – (iii)

$$\begin{aligned} \frac{2}{N} \sum_{n=0}^{N-1} \epsilon_k \cos(\omega_k n T_s) &= \frac{2}{N} \sum_{n=0}^{N-1} \mathcal{N}(0, \sigma) \cos(\omega_k n T_s) \\ &= \frac{2}{N} \Phi_{1-\alpha} \frac{\sigma}{\sqrt{N}} \sum_{n=0}^{N-1} \cos(\omega_k n T_s) \end{aligned} \quad (\text{A.19})$$

$$\begin{aligned} &< \Phi_{1-\alpha} \frac{2\sigma}{\sqrt{N}} \\ \epsilon_{\text{FS}} &< \Phi_{1-\alpha} \frac{2\sigma}{\sqrt{N}} \end{aligned} \quad (\text{A.20})$$

corresponds to the sampling error, which might be encountered in real measurements. Given a normal distributed error function $\epsilon_k = \mathcal{N}(0, \sigma)$ with $\Phi_{1-\alpha}$ as the corresponding quantil, it turns out, that this error suffice Equation (A.20) and vanishes in the limit $N \rightarrow \infty$. This is valid because a linear combination of normally distributed variables keeps normally distributed, see Parzen Parzen (1962, Theorem 4A, p. 90). And in addition, expression (A.20) gives the upper limit of the parameter confidence interval.

In summary, the estimation of Fourier coefficients a_k (and b_k)

$$\frac{2}{N} \sum_{n=0}^{N-1} s_w(n T_s) \cos(\omega_k n T_s) \approx a_k \left(1 + \frac{\Delta \varphi}{T} \right) \pm \Phi_{1-\alpha} \frac{2\sigma}{\sqrt{N}} \quad (\text{A.21})$$

is affected by the truncation error with respect to the full period of ω_k and a random error from the measurement. The first is independent from the sampling which proves that Fourier decomposition is a non consistent estimator for amplitude and frequency. The last term, the random error, converges to zero in the limit of large N , as expected.

B Table of Significant Periods

Table 3: Significant peaks of the sun spot spectrum

ID	$P_{\text{Yrs}}/\text{Yrs}$	$\pm\Delta P/\text{Yrs}$	$\frac{f_{\text{Lat}}}{10^{-2}\cdot\text{deg}}$	PSD	$\log_{10}(p)$
1	559.540	216.060	-3.170	0.001	-23
2	358.855	266.266	2.946	0.001	-34
3	162.651	505.535	-1.225	0.004	j -50
4	155.909	382.298	1.159	0.004	j -50
5	124.893	142.836	5.426	0.001	-29
6	84.992	47.192	7.824	0.001	-23
7	79.902	40.544	10.649	0.000	-13
8	77.974	38.225	-1.862	0.008	j -50
9	75.367	35.247	1.453	0.005	j -50
10	73.676	33.410	-4.656	0.000	-19
11	73.497	33.219	-12.487	0.000	-13
12	68.258	27.982	3.916	0.001	-48
13	65.974	25.892	13.117	0.000	-15
14	51.097	14.731	-1.593	0.006	j -50
15	50.375	14.287	1.408	0.003	j -50
16	47.212	12.436	-5.263	0.001	-39
17	37.254	7.557	4.246	0.001	-24
18	36.892	7.406	-1.124	0.018	j -50
19	36.798	7.366	1.525	0.011	j -50
20	35.530	6.850	-5.557	0.001	-43
21	34.615	6.490	-11.245	0.000	-18
22	32.852	5.826	9.391	0.000	-15
23	29.882	4.795	1.386	0.008	j -50
24	27.718	4.111	13.915	0.001	-26
25	27.203	3.956	-4.189	0.004	j -50
26	27.126	3.934	6.638	0.001	-26
27	26.750	3.823	3.881	0.001	-43
28	26.408	3.724	-1.324	0.055	j -50
29	26.283	3.688	1.207	0.044	j -50
30	23.924	3.046	18.856	0.001	-27
31	23.816	3.018	-18.655	0.000	-11
32	21.684	2.495	-1.082	0.600	j -50
33	21.637	2.484	1.152	0.607	j -50
34	21.284	2.403	-6.092	0.004	j -50
35	16.976	1.522	1.965	0.003	j -50
36	16.936	1.514	-2.713	0.003	j -50
37	15.424	1.254	1.160	0.018	j -50
38	15.363	1.244	-1.365	0.017	j -50
39	13.123	0.906	-3.694	0.001	j -50

40	12.836	0.867	1.075	0.016	j	-50
41	12.819	0.865	-1.303	0.017	j	-50
42	10.668	0.598	2.450	0.002	j	-50
43	10.275	0.555	-3.534	0.001	j	-50
44	10.106	0.537	0.982	0.003	j	-50
45	9.495	0.473	1.616	0.002	j	-50
46	8.994	0.425	-3.782	0.002	j	-50
47	8.980	0.423	-1.204	0.008	j	-50
48	7.711	0.312	-0.948	0.012	j	-50
49	7.704	0.311	1.414	0.010	j	-50
50	7.207	0.272	1.210	0.026	j	-50
51	7.195	0.272	-1.164	0.026	j	-50
52	7.181	0.271	2.910	0.021	j	-50
53	6.375	0.213	-2.583	0.004	j	-50
54	5.919	0.184	2.345	0.003	j	-50
55	5.891	0.182	-2.916	0.002	j	-50
56	5.638	0.167	2.907	0.002	j	-50
57	4.558	0.109	-2.872	0.003	j	-50
58	4.310	0.097	3.558	0.002	j	-50
59	4.247	0.095	-2.963	0.003	j	-50
60	4.125	0.089	-3.366	0.002	j	-50
61	4.065	0.087	3.815	0.002	j	-50
62	3.944	0.081	-3.364	0.002	j	-50
